# Liquid Crystal Templated Chiral Plasmonic Films with Dynamic Tunability and Moldability

*Dorota Grzelak, Martyna Tupikowska, David Vila-Liarte, Dominik Beutel, Maciej Bagiński, Sylwia Parzyszek, Monika Góra, Carsten Rockstuhl, Luis M. Liz-Marzán, and Wiktor Lewandowski\**

Thin films sustaining plasmonic circular dichroism (PCD) have acquired high scientific relevance and a great potential for applications. While most efforts in PCD thin film structures focus on lithographically fabricated static metasurfaces, the bottom-up fabrication of active chiral plasmonic films constitutes an alternative approach. Herein, the preparation of PCD thin films by melting and freezing a mixture of liquid crystal (LC), a chiral dopant, and gold nanoparticles (Au NPs), serving as helical matrix, symmetry breaking inducer, and plasmonic component, respectively is reported. UV–vis and circular dichroism spectroscopies, as well as theoretical modeling are used to disclose the interactions among thin film components, toward maximizing the PCD dissymmetry factor (g-factor). Variation of substrate temperature affords reversible off/on switching of the chiroptical response. The soft nature of LC matrix enables patterning of the films via a thermal nanoimprinting method, using a polydimethylsiloxane mold for transfer-printing onto a flexible substrate, leading to stretchable PCD films. The PCD wavelengths can be readily tuned by varying the geometry of the Au NPs. This work provides an efficient technique to produce PCD thin films with active plasmonic properties and mechanical tunability.

## 1. Introduction

Chiral thin films possess outstanding features such as chiral light absorption and emission, with practical implications for the current and next generation optoelectronic technologies. For example, thin films exhibiting circular dichroism (CD) or circularly polarized luminescence have been widely studied to realize novel types of organic light-emitting diodes, polarizers, and organic field-effect transistors.[1–6] Meeting the requirements for particular applications requires tuning the chiroptical properties of the films, which is possible through a rational choice of building blocks and control over the symmetry and geometry of the film. Thus, it is not surprising that soft organic matter has been a primary choice, owing to its processability, self-assembly, and possibilities for mesoscopic morphology control.[7–10] A transformative leap in advancing the properties and applications of chiral thin films is currently foreseen by incorporating inorganic nanoscale building blocks, which exhibit enhanced light-matter interactions.[11–15] Chiral thin films comprising semiconductor nanostructures have been extensively studied toward increasing efficiency, tuning wavelength range, and unlocking new applications.[16–20] Much slower advancement has been however achieved for thin films containing metal nanoparticles, in which chiral assembly of plasmonic nanoparticles may lead to plasmonic circular dichroism (PCD), an essential feature for precise control over chiroptical properties in the visible and near-infra red (IR) wavelength range.[21,22]

D. Grzelak, M. Tupikowska, M. Bagiński, S. Parzyszek, M. Góra, W. Lewandowski
Faculty of Chemistry
University of Warsaw
Ludwika Pasteura 1, Warsaw 02-093, Poland
E-mail: wlewandowski@chem.uw.edu.pl

The ORCID identification number(s) for the author(s) of this article can be found under https://doi.org/10.1002/adfm.202111280.

D. Vila-Liarte, L. M. Liz-Marzán
CIC biomaGUNE
Basque Research and Technology Alliance (BRTA)
Paseo de Miramón 194, Donostia-San Sebastián 20014, Spain

D. Vila-Liarte, L. M. Liz-Marzán
Centro de Investigación Biomédica en Red
Bioingeniería, Biomateriales y Nanomedicina (CIBER-BBN)
Paseo de Miramón 194, Donostia-San Sebastián 20014, Spain

D. Beutel, C. Rockstuhl
Institute of Theoretical Solid State Physics
Karlsruhe Institute of Technology
Karlsruhe 76131, Germany

C. Rockstuhl
Institute of Nanotechnology, Karlsruhe Institute of Technology
Karlsruhe 76021, Germany

L. M. Liz-Marzán
Ikerbasque
Basque Foundation for Science
Bilbao 48009, Spain

The main challenge for achieving PCD in thin films is the limited number of available synthetic approaches to tunable materials. On one hand, PCD can be readily achieved in colloidal, mostly aqueous systems, by means of bottom-up approaches. These approaches ensure scalability, fabrication fidelity,[23–25] and active switchability.[26–28] However, removing the solvent hinders tunability and generally has a destructive impact on PCD.[29] On the other hand, top-down lithographic approaches provide access to ultrathin PCD metasurfaces that offer strong and broadband chiral response.[30,31] It happens, however, at the expense of long fabrication times and limited availability of building blocks with different morphologies. Obtaining composites of metal NPs and chiral soft matter matrices by combined soft lithography and bottom-up approaches might be the way to resolve these issues, as they provide efficient, universal, and scalable preparation methods of PCD materials, thereby advancing toward their integration into flexible photonic devices.[32] Among the different available templates or host matrices that may potentially meet the requirements for such purposes,[17] liquid crystals are particularly interesting as some phases exhibit high optical and structural asymmetry, as well as remarkable stimuli responsiveness.[20,33–40]

We have recently shown that the synergic combination of plasmonic properties of NPs and LC phases showing mesoscopic chirality offers a unique strategy to access PCD films. Shortly, chiral morphology in LCs can arise from the assembly of bent, achiral molecules that form frustrated molecular layers twisting into helical nanofilaments (HNF) with mesoscale dimensions. When HNFs are doped with NPs, controlled freezing from the isotropic phase leads to the formation of double-helical NP superstructures, which replicate the morphology of the organic HNF.[41] However, the spontaneous symmetry breaking of the HNF phase meets the inconvenience of lacking a preferential handedness, which represents an unsolved challenge in various systems based on the templated assembly of achiral plasmonic units.[42] We have also shown that, in HNF/NP thin films, PCD can be detected in micrometer-sized domains composed of single-handed helices.[43] Although selective removal of one helicity leads to a macroscopic PCD response, the imperfection of the deracemization method limits the achievable CD activity. Non-preferential symmetry breaking was also found to be detrimental against active switchability.

In this work, we propose the utilization of chirality transfer and amplification from a minority amount of a chiral additive toward acquiring homochiral thin films with strong PCD response on the bulk scale, where we observe chirality propagation through several length scales—from a chiral molecular dopant, through an organic supramolecular structure, and ultimately to a chiral NP assembly. We present a comprehensive study of the optimization of nanocomposite composition and analysis of mutual interactions between its constituents, leading to the optimization of the PCD response using a minor amount of chiral molecules. Following this approach, we aimed at unlocking new applications in flexible optoelectronics by gaining LC softness, endurance, stimuli responsiveness, and moldability. To this end, we employed polydimethylsiloxane (PDMS)-based thermal nanoimprinting and transfer printing as highly versatile techniques for heterogeneous integration of photonic devices with other optical components and electronic circuits, on both rigid and flexible

substrates.[44,45] As a result, we developed a versatile material with tailored, dynamically controlled chiroptical properties through successful use of the characteristics of soft matter to preserve its features during mechanical patterning and stretching.

## 2. Results and Discussion

### 2.1. Design and Fabrication of Chiral Nanocomposites

To fabricate the proposed chiral PCD thin films, we first devised and synthesized a new liquid crystalline compound serving as the matrix for NP organization, namely 1,3-phenylenebis[4-(4-oleyloxy-phenyliminonetyl)benzoate] (Oleyl-Imine-Matrix, OIM, **Figure 1**a, Note S1, Figure S2, Supporting Information). We hypothesized that OIM design would ensure the formation of HNF, a relatively low melting temperature, and controllable macroscopic chirality via chirality transfer and amplification. A detailed discussion on the benefits of using OIM is given in Note S2, Supporting Information. To determine the phase behavior of the OIM compound, we used polarizing optical microscopy (POM, Figures S3 and S4, Supporting Information) and differential scanning calorimetry (Figure S5, Supporting Information). The obtained results indicate that at 130 °C, on cooling from the isotropic melt, OIM forms a B7 phase.[46] Further cooling, below 120 °C, affords a dark conglomerate phase, apparently a mixture of right and left-handed helical domains. The microscopic texture of the dark conglomerate appears completely dark under crossed polarizers, while on uncrossing the polarizers, the phase usually exhibits a conglomerate structure with chiral domains of opposite handedness. This suggests that the phase arises from the assembly of curved molecular layers with microscale domains, formed by a spontaneous chiral resolution. Depending on the type of the layer curvature various morphologies of the phase can be achieved, for example, among others, sponge-like,[47] HNF,[48] or heliconical-layered nanocylinders.[49] To unequivocally determine the mesoscopic morphology of the dark conglomerate phase, transmission electron microscopy (TEM) was used. TEM images of a drop-casted and heat-annealed (i.e., heated above the isotropization point and then cooled down back to room temperature at 20 K min$^{-1}$) material revealed helical nanofibers with dimensions characteristic of LC HNFs:[50–53] Pitch $p \approx 230$ nm, width $w \approx 45$ nm, thickness $z \approx 15$ nm (Figure 1c). OIM nanofibers formed dendritic domains, suggesting that fibers in a single domain grow from a single nucleation point upon freezing.[41] Notably, helices preserve the handedness during dendritic growth, which in the case of an achiral liquid crystal leads to a conglomerate structure—a random mixture of domains comprising either left- or right-handed HNF.

Since we aimed at controlling film chirality on a bulk scale, we decided to dope the material with either (S)-(4)[(Methylheptyloxy)carbonyl]phenyl-4′-octyloxy-4-biphenylcarbohylate (dopS) or its R-enantiomer (dopR), that is, chiral, low molecular weight compounds (Figure 1a,b), which have previously been used for similar purposes.[54,55] UV–vis measurements of the tetrahydrofuran (THF) solutions of the dopant compounds and OIM revealed single, narrow absorption peaks centered at
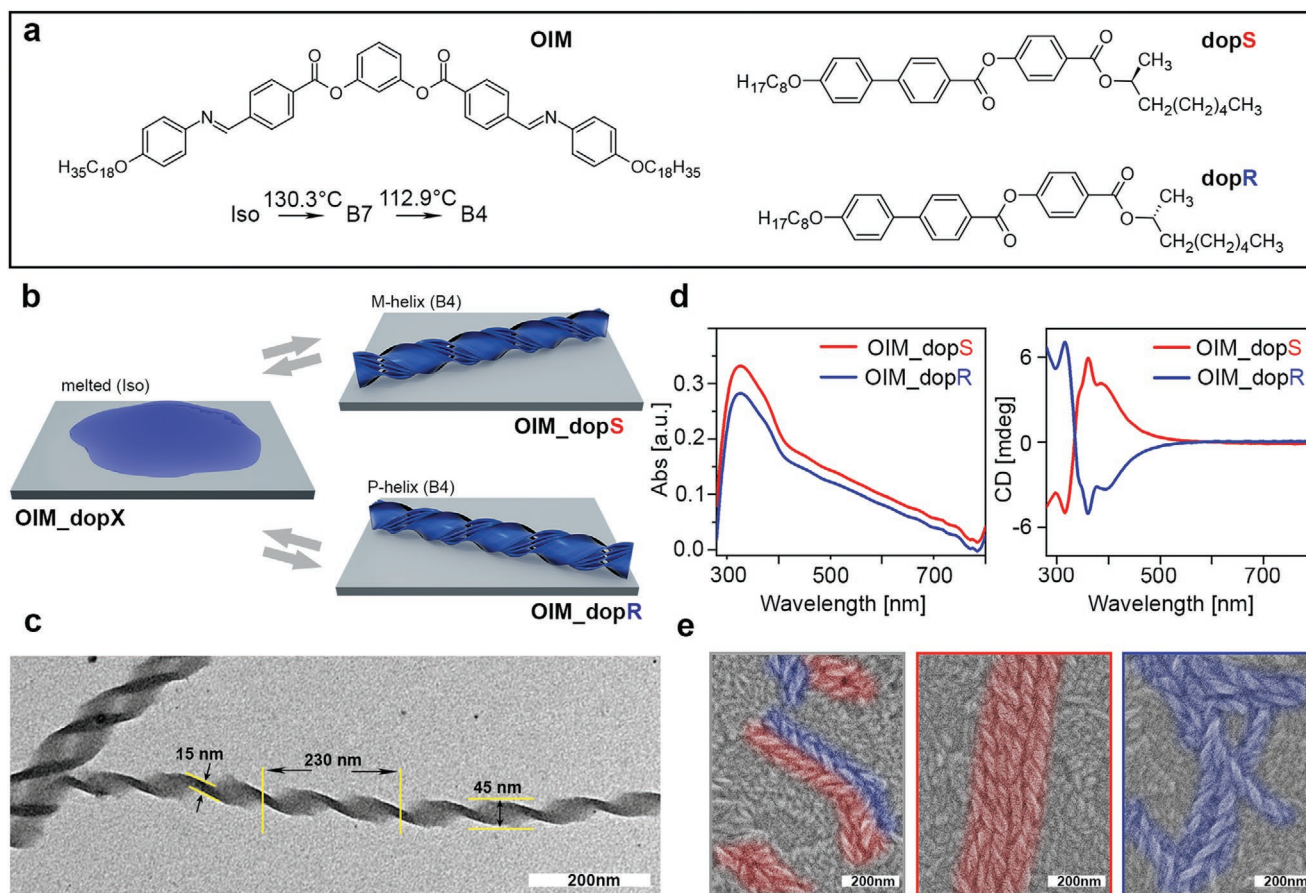
**Figure 1.** Controlling the chirality of the liquid crystalline matrix. a) Molecular structures of compounds used in this work. OIM: Liquid crystal used as the matrix; dopS and dopR: Enantiomers of dopants used to control matrix chirality. b) Scheme of the preferential formation of right-handed (P-type) and left-handed (M-type) helical nanofibers in OIM_dopR and OIM_dopS mixtures, respectively. c) TEM image of a helical nanofiber formed by OIM (without dopant). Pitch, diameter, and width of the helix are indicated. d) UV–vis extinction and circular dichroism spectra of thin films of OIM_dopS and OIM_dopR mixtures, indicated with red and blue colors, respectively. e) Scanning electron microscopy images showing M- and P-helices formed in, from left to right: OIM (without dopant), OIM_dopR, and OIM_dopS mixtures; M- and P-helices are falsely colored in red and blue, respectively.

≈320 and 400 nm, respectively (Figure S6, Supporting Information). UV–vis measurements of heat-annealed films comprising OIM matrix with either of the dopants (10 wt%) were almost identical, with two absorption bands centered at 320 nm and 350 nm. Conversely, circular dichroism (CD) spectra recorded for OIM films doped with dopR and dopS enantiomers were mirror images, with bands centered at ≈330 and ≈360 nm; the bands were positive/negative for R dopant and negative/positive for S dopant, respectively (Figure 1d). In both cases, zero-crossing at 350 nm was observed. Additionally, a band centered at ≈400 nm was also revealed, which has been ascribed to the formation of helical nanofilaments in HNF phases.[56] These measurements attested the possibility of achieving preferential symmetry breaking, that is, enantiomeric excess of a given handedness of helical nanofibers in a cm-scale thin film. Scanning electron microscopy (SEM) provided further evidence for this hypothesis, by revealing fibers with both handedness in an undoped sample. In contrast, helices with a single handedness were imaged in samples doped with either enantiomeric form of the chiral dopant (Figure 1e, Figures S7–S12, Supporting Information).

At this point, it is worth highlighting that CD measurements of thin films can be prone to linear optical effects (linear birefringence, linear dichroism etc.).[6] Thus, for all samples presented in this manuscript, we performed a POM measurement to exclude a significant level of birefringence, CD measurements being averaged over a series of measurements for rotated samples (Figures S13–S17, Supporting Information). Also, measurements of flipped samples (from the "back" side, data not shown) were performed. No sign reversal of the CD bands was observed.

As a final component of the composites, we prepared gold nanoparticles capped with a mixed monolayer of dodecane- and liquid-crystal-like thiols (Note S1, Figure S1, Supporting Information). Such a mixed design of the organic coating for the NPs was previously shown to enable efficient mixing of NPs with the LC host.[41,57–59] The synthesized NPs were uniform in size, with an average diameter of 14.5 ± 1.6 nm (Au15), as confirmed by TEM analysis (Note S4, Figure S25, Supporting Information). In THF dispersion, these NPs exhibited an extinction band centered at ≈520 nm (Figure S27, Supporting Information) due to a localized surface plasmon resonance
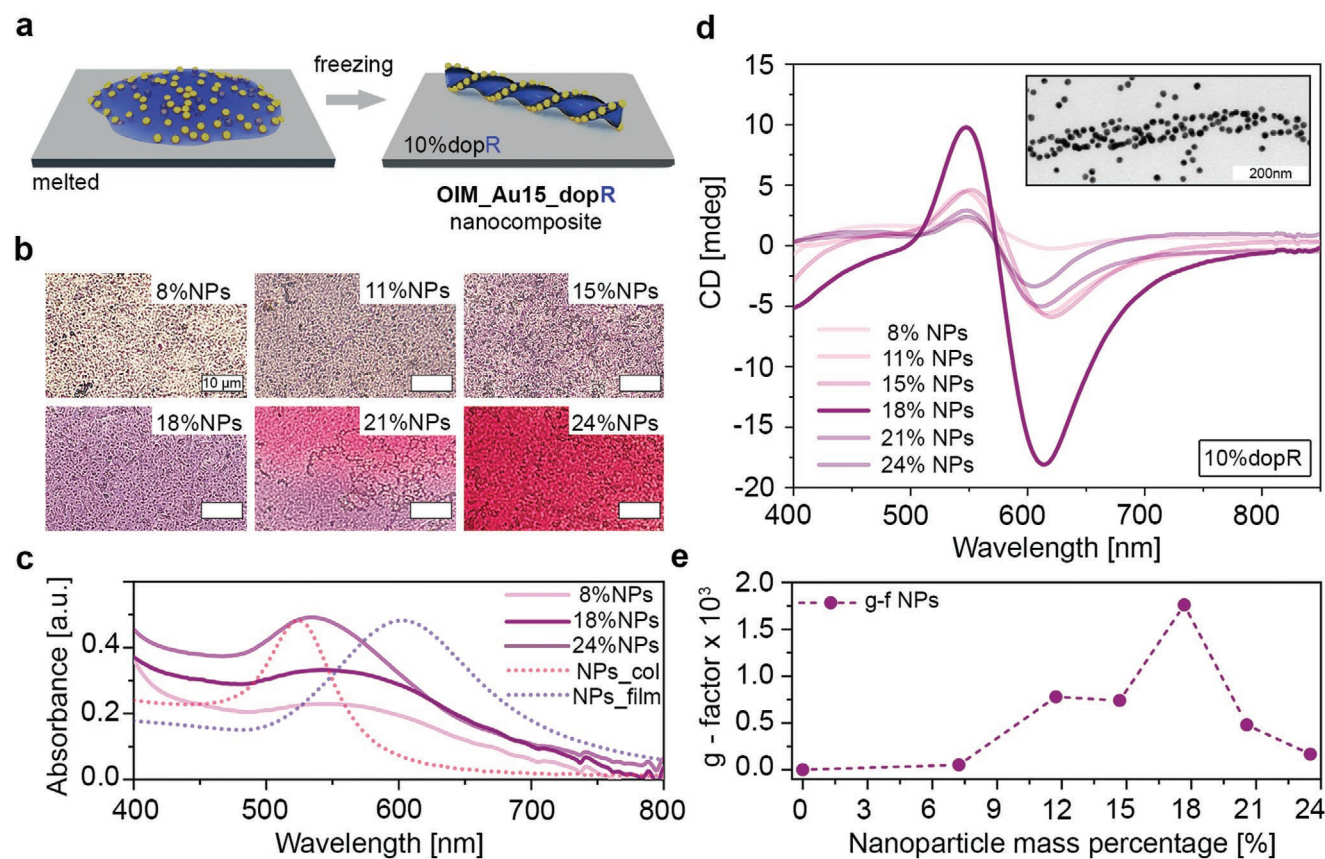
**Figure 2.** Optimization of Au15 content in chiral nanocomposites. a) Scheme for the formation of left-handed helical nanofibers decorated with Au NPs upon freezing of OIM_Au15_dopR films. b) Optical images of films made of OIM_Au15_dopR samples on glass slides, with varying Au15 content (wt% of Au15 in each composites is indicated). c) UV–vis extinction spectra of thin films of OIM_Au15_dopR, for selected samples from panel b (solid lines); UV–vis extinction spectra of Au15 dispersion in toluene and thin films of Au15 are shown for comparison (dashed lines). d) Circular dichroism spectra for all samples shown in panel b; the inset shows a representative TEM image revealing closely packed Au15 decorating a helical nanofilament, as well as loosely distributed Au15, not deposited on helices. e) Anisotropy factor (g-factor) calculated at the maxima of the minus CD plasmonic band (≈600–610 nm) for samples shown in panel d.

(LSPR) characteristic of well-separated, uncoupled Au NPs, endowing the dispersion with a red color. The LSPR position red-shifted to 610 nm upon dropcasting, thereby endowing the films with a blueish color, characteristic of closely packed Au NPs with efficient inter-particle plasmon coupling in the film state. Efficient plasmon coupling is important, given the achiral nature of individual NPs. In such a case, chiral oscillations of plasmons require chiral arrangements of coupled NPs.[60]

## 2.2. Optimization of Chiral Plasmonic Film Composition

To prepare and optimize the content of chiral plasmonic composites, a series of THF solutions with judiciously chosen OIM/dopR ratio were first prepared. Varying amounts of Au15 NPs (8–24 wt%) were then added to the solutions. Finally, the obtained samples were dropcasted onto glass slides, melted, and cooled in a controlled way (20 K min$^{-1}$, Figure S20, Supporting Information) to prepare chiral composites, OIM_Au15_dopR (**Figure 2**a).

Color differences were clearly observed among the prepared OIM_Au15_dopR composite films with varying Au NP content.

On increasing the weight fraction of Au15 NPs up to 18%, the samples gradually became purple, whereas films with a higher NP content were reddish (Figure 2b, further comments can be found in Note S5, Supporting Information). These observations were in agreement with UV–vis extinction spectra of OIM_Au15_dopR samples (Figure 2c). We recorded LSPR bands in the visible range ($\lambda_{max}$ between 500 and 600 nm). For samples comprising up to 18 wt% Au15, broadening of the bands (FWHM ≈ 250 nm) reflected the overlap of contributions from coupled and isolated fractions of NPs. A higher content of NPs (21, 24 wt%) translated into a significant blueshift and narrowing of the plasmon band (FWHM ≈ 120 nm), indicating an increasing content of isolated, uncoupled Au NPs (Figure S28, Supporting Information). A representative TEM image for OIM_Au15_dopR with 18 wt% Au confirmed this hypothesis by revealing closely packed Au15 deposited onto helices, next to well-separated Au15 NPs outside of the helices (Figure 2d inset).

CD spectroscopy was used to probe PCD in OIM_Au15_dopR thin films. The CD spectra featured characteristic bands for the OIM_dopR mixture and additional, more intense (plasmonic) bands in the visible region: A positive band centered
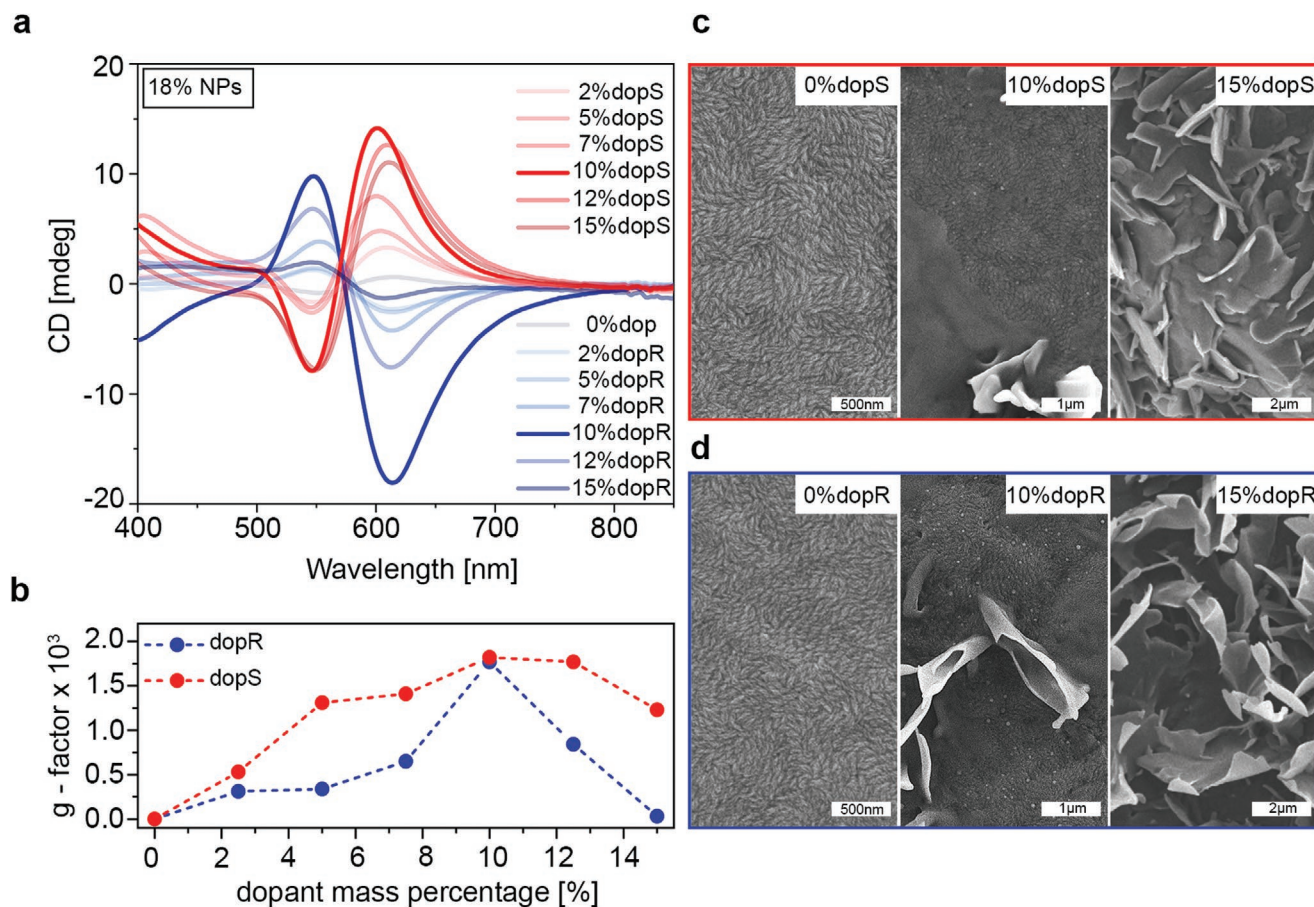
**ADVANCED
SCIENCE NEWS**

www.advancedsciencenews.com

**ADVANCED
FUNCTIONAL
MATERIALS**

www.afm-journal.de

**Figure 3.** Controlled chirality amplification and transfer. a) CD spectra for increasing (0–15%) dopR (blue) and dopS (red) mass percentage in OIM_Au15_dopX (X = R or S) nanocomposite. b) Maximum g-factor value for the plasmonic CD band, for selected dopR (blue) and dopS (red) mass percentages in OIM_Au15_dopX nanocomposites. c) SEM images of OIM_Au15_dopS nanocomposite thin films, for 0, 10, and 15 wt% dopS. d) SEM images of OIM_Au15_dopR nanocomposite thin films, for 0, 10, and 15 wt% dopR.

at ≈550 nm and a negative band ≈610 nm, with zero-crossing at ≈570 nm (Figure 2d). The position of the zero-crossing was the same for all samples. The position of the zero-crossing corresponds to the absorption band maxima position for non-polarized light. The redshift from the plasmon band observed in NP dispersions is in agreement with our interpretation of UV–vis data, regarding the presence of different fractions with coupled and non-coupled NPs, only the former contributing to the CD response. The measured ellipticity reached a maximum for a sample comprising 18 wt% Au15 NPs. Further increase in the amount of NPs resulted in a decrease in signal strength, suggesting at least partial inhibition of HNF formation. Calculated g-factors (see Equation (S1), Supporting Information) at the minus band maxima (Figure 2e) confirmed this trend. From these results, we conclude that 18 wt% was the optimal content of Au15 NPs, and, therefore, we used this doping rate in all further investigations. This conclusion was important toward optimizing the CD response, since helical arrangements of spherical NPs can induce chiral far-field properties only if plasmonic coupling occurs.

Next, we optimized the amount of chiral dopant in the mixture (2–15 wt%), using the optimized amount of Au15. The acquired CD spectra from the resulting film nanocomposites,

OIM_Au15_dopX (X = R or S), doped with either dopR or dopS, were mirror images with the sign of the bands not being affected by the amount of dopant (**Figure 3**a). We also note a correlation between the signs of organic and plasmonic bands, suggesting that the CD response of plasmonic nanocomposites correlates with the handedness of helical nanofibers (Figure 3b, Figures S30 and S31, Supporting Information). By increasing the mass percentage of either of the dopants, we observed a gradual enhancement in the measured CD signals and g-factors, up to 10 wt% dopant. In contrast, for 12 and 15 wt%, we observed a significant decrease in the measured CD signals and g-factors (Figure 3c). To understand these observations, we performed SEM analysis on representative samples of OIM without dopants and with 10 and 15 wt% of either dopS or dopR (Figure 3d,e). SEM micrographs of OIM show a wavy structure, characteristic of HNFs, covering the entire imaged area. With the addition of 10 wt% dopX, the imaged surface was partly covered with organic matter forming layers. Samples containing 15 wt% dopant show a surface entirely covered with similar layered structures. We hypothesize that the observed layered crystals are formed by the dopants themselves, phase separating on the surface of HNFs during freezing of the material. The optimal doping value was thus around 10 wt%, which
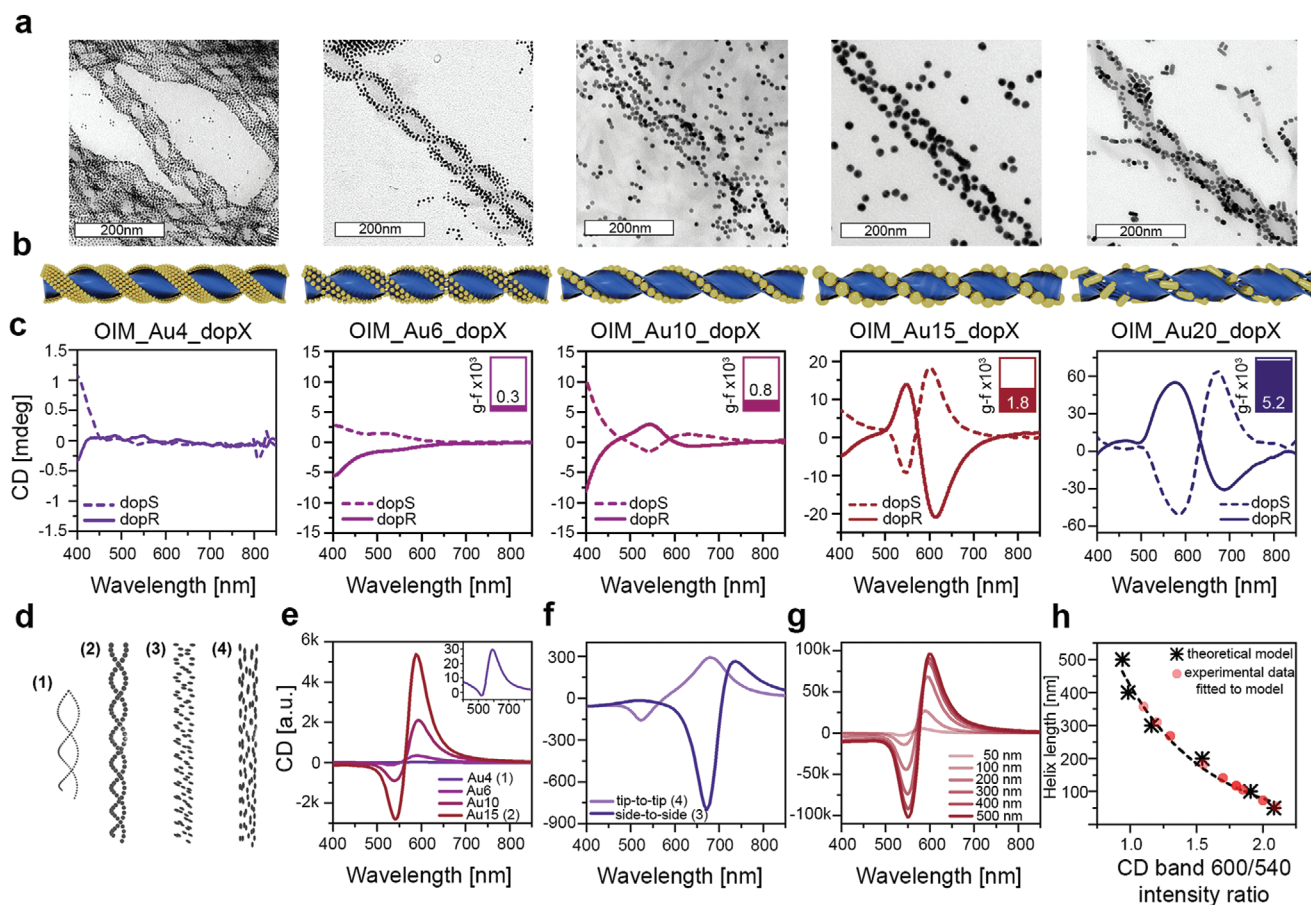
**Figure 4.** OIM as a matrix for nanoparticles with different sizes and shapes. a) TEM images of helical arrangements of Au NPs with different size and shape; note that the apparent spherical shape of NRs is due to their vertical orientation. b) 3D models of single helices of chiral composites corresponding to TEM images in (a). c) CD spectra of chiral OIM-based nanocomposites with either dopR (solid lines) or dopS (dashed lines), prepared using (from left to right): 4, 6, 10, and 15 nm spherical Au NPs, and 8 × 20 nm Au NRs; these NPs are called Au4, Au6, Au10 and Au20, respectively. Insets in the spectra indicate the mean g-factor values calculated for a given NP type, using data for either handedness. d) Models of the helical arrangements of nanoparticles used for theoretical modeling: 1) Helix of 4 nm diameter Au NPs, enlarged for clarity; 2) helix of 15 nm diameter Au NPs; 3) helix of Au NRs oriented side-by-side; 4) helix of NRs oriented tip-to-tip. e) Numerical modeling for chiral spherical nanoparticle arrangements into helices of 100 nm length for different NP sizes, as used in the experiments; inset shows the signal for 4 nm diameter NPs. f) Theoretical modeling for different chiral arrangements (shown in panel d) of 40 Au NRs with dimensions corresponding to Au20. g) Theoretical modeling of the CD response for helices with different lengths, built from 15 nm diameter NPs, normalized for a fixed amount of gold. h) CD band 600/540 intensity ratios for increasing lengths of helical arrangements of 15 nm diameter NPs; theoretically calculated data (stars) were fitted with a second order polynomial (dashed curve), on which points corresponding to 15 experimentally derived intensity ratios were overlaid.

induces maximum enantiomeric excess without disturbing the HNF structure. Higher dopX content either disturbed the creation/crystallization process of HNFs or covered their surface, thereby obscuring the helical structure and its interaction with incident light by additional birefringence.

### 2.3. Chiral Plasmonic Films with Different Nanoparticles

To test if the OIM organic matrix can host different NPs, we prepared ≈4 (Au4), ≈6 (Au6), and ≈10 (Au10) nm diameter spherical Au NPs, as well as 8 × 20 nm (Au20) gold nanorods (NRs). Depending on the size of spherical NPs, a PCD response with variable intensity was expected, while the different geometry of Au NRs should enable fine tuning of the wavelengths at which PCD response is observed. All NPs were synthesized

using literature protocols;[61–64] spherical nanocrystals were covered with a mixed monolayer of aliphatic and LC thiols, similar to Au15. On the other hand, gold NRs were covered exclusively with the LC-like ligand, so as to ensure efficient phase transfer from an aqueous phase. More details on the synthesis and morphology of NPs can be found in Note S4, Supporting Information (Figures S22–S26, Supporting Information).

OIM_AuNPs_dopX nanocomposites comprising 18 wt% NPs were then prepared and heat annealed. TEM images of the resulting thin films again revealed double-helical assemblies of Au nanocrystals (**Figure 4**a). Interestingly, Au10 and Au15 NPs formed helically twisted 1D chains, while Au4 NPs formed helically twisted 2D ribbons since several NPs could fit across the HNF edge (Figure 4b). In the case of Au20 NRs, TEM images revealed the presence of various geometries of NR arrangement, including side-to-side and tip-to-tip assemblies (Figure 4a

and Figure S29, Supporting Information), with individual NRs deposited outside of organic helices showing a rod-like shape with aspect ratio similar to the NRs before heat annealing. This observation allows us to conclude, that NRs retain their elongated shape after melting/freezing of the composite. We then measured the CD signal to test how the changes in size and morphology of the assembled NPs translate into the PCD response (Figure 4c). CD spectra of films comprising Au4 NPs did not exhibit PCD. For larger NPs, a positive correlation between NP size and PCD intensity was observed, as expected, with similar characteristics of the signals. In the case of Au20, plasmonic Cotton bands were evidenced, centered at 590 and 690 nm. The signs of the lower and higher wavelength bands were analogous to those in films comprising spherical NPs. Zero-crossing between Cotton bands for Au NRs was found at ≈650 nm. It is worth noting that the latter value, representing $\lambda_{max}$ of the absorption band responsible for PCD response, is blueshifted with respect to the longitudinal LSPR $\lambda_{max}$ of Au NRs in dispersion. This suggests that NRs preferentially couple side-to-side in the film,[65] in agreement with TEM images. It should be noted that the ability of the OIM matrix to host various Au NPs of different sizes seems to mainly depend on the surface coating of the particles. This allows us to speculate that different metallic and semiconductor NPs, with sizes comparable to or smaller than the grain boundary size (thickness of the HNF), should form helical assemblies if doped into the matrix.

To fully understand the PCD response, we performed simulations based on the T-matrix method[66] using double helices made of equally-spaced NPs as computational models. Such models were constructed by using mean dimensions of the helices, NP sizes, and interparticle distances calculated from TEM images (Table S1, Supporting Information). In the simulation, a double helix made of gold NPs (Figure 4d), embedded in a uniform medium with constant refractive index 1.5 (corresponding to the LC matrix and organic medium), was illuminated orthogonally to its main axis. The geometry of illumination was chosen to represent the experimental set-up, as a glass substrate is placed perpendicular to the measurement light beam and HNFs tend to grow parallel to the plane of the substrate (Figure 3d,e). A clear PCD response was detected in all studied cases, with a positive correlation between the strength of the CD bands and sizes of spherical NPs (Figure 4e), similar to the experimental results. It should be noted that, in the case of the smallest spherical nanocrystals (Au4), the calculated PCD signal was 3 orders of magnitude weaker than that for Au15, likely below the sensitivity of the CD spectrophotometer. The corresponding theoretical analysis was performed as well for a helical arrangement of gold ellipsoids with dimensions used in the experiment, and their chiroptical response has been studied analogously. Three different arrangements were considered: side-by-side and tip-to-tip (3 and 4 in Figure 4d, respectively), and tangential to helical axis (see Figures S34 and S35, Supporting Information). As shown in Figure 4f, the strength, shape, and position of the simulated CD peaks vary substantially between the considered arrangements, showing a strong correlation of the simulated spectra for the side-to-side arrangement with experimental data, although contributions from other arrangements should also be considered given the

previously discussed TEM images of the sample. This phenomenon was previously reported for semiconductor nanorods.[67] A few different lengths of helical assemblies of Au15 were tested to verify if this parameter changes the characteristics of PCD signals (Figure 4g). Modeled spectra exhibited the Cotton effect with signs and positions of the bands perfectly matching the experimental results. The length of the twisted clusters did affect both the intensity of CD response (the longer the cluster, the higher the intensity) and the signal intensity ratios between positive and negative bands in the spectra, as shown in Figure 4h (Figure S36, Supporting Information, for different NP sizes). The signal intensity ratios calculated from experimental data for 15 samples of OIM_Au15_dopX (Note S7, Table S2, Supporting Information) suggest that the length of the helically arranged NP clusters varies from 50 to 350 nm, as shown in Figure 4h. Additionally, we observed that a longer helix dimension did not affect the positions of the CD bands. In Figure 4h we also observe, that the shorter helices show a larger dissymmetry between the positive and the negative peak. This can probably be explained by the larger influence of boundary effects from the ends of the helices on the total response.

To verify whether the orientation of the illumination may affect the response, a sweep over different incident angles, 0° to 90° was performed for an assembly of 15 nm diameter NPs (Figure S37, Supporting Information, 0° and 90° corresponds to illumination perpendicular and parallel to the main axis of HNF, respectively). Notably, when considering a mean value calculated for tilts between 0° and 30°, that is, including helices that could tilt at domain edges, the characteristic response was very similar to that at 0° discussed above. Interestingly, a sample illuminated along the main axis exhibited a much stronger PCD response and sign inversion, suggesting that orientational control over the helices could afford PCD films with an order of magnitude stronger response and switchable CD sign, which should be considered for future research endeavors. It should be noted that a similar variation of the CD response, by modification of the helices illumination geometry, was previously reported for other helical assemblies of NPs.[68,69]

## 2.4. Active Chiral Plasmonics

We next tested whether the soft, responsive character of the LC matrix, expressed through the phase sequence shown in Figure 1a, can translate into responsiveness toward external stimuli of the chiral, composite thin films. We therefore measured CD spectra of thin films comprising Au15 and Au20 at 25 and 155 °C, corresponding to HNF and Iso phases of the OIM matrix, respectively. We hypothesized that freezing/melting the nanocomposite (**Figures 5**a,d) would enable reversible on/off switching of the PCD properties. Temperature-dependent CD spectroscopy measurements were performed by attaching glass slides covered with thin films to a heating stage that allows for transmission measurements over a 2 mm diameter circular area, and then mounting the stage within the far-field CD spectrophotometer. Figure 5b,e show representative CD spectra of the tested samples after drop casting and melting (dashed curves) and then freezing (solid curves). At the molten state, no CD signals were recorded between ≈400 and 900 nm. The
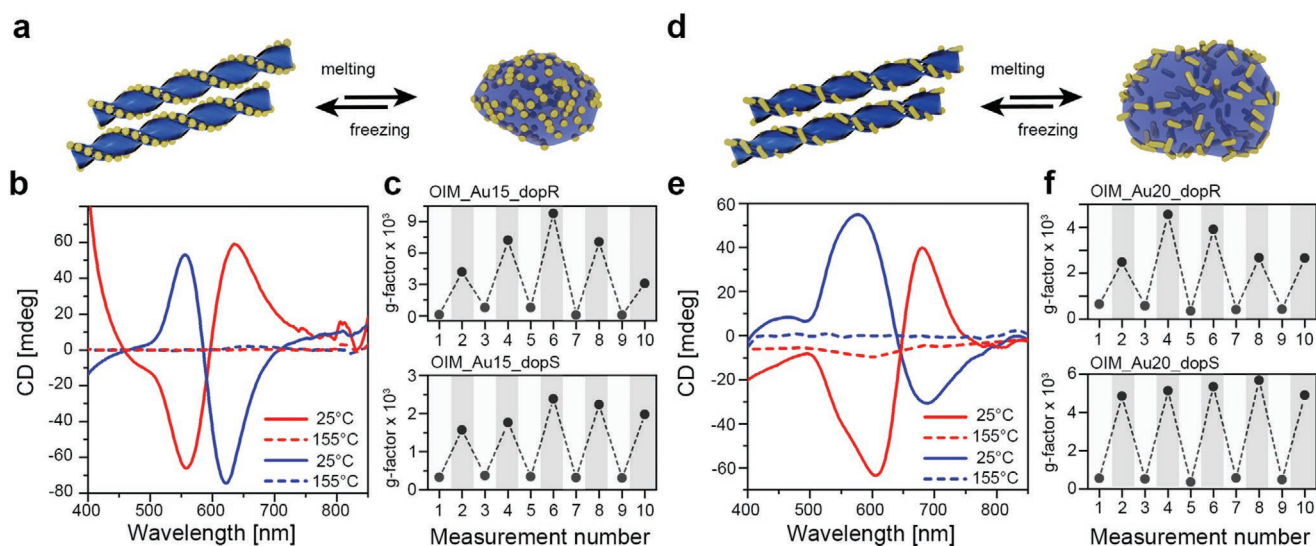
**Figure 5.** Dynamic reconfigurability of OIM-based chiral thin films. a) Schematic model of OIM_Au15_dopX material structure on thermal melting/freezing. b) CD spectra for OIM_Au15_dopR (blue line) and OIM_Au15_dopS (red line) thin films at 25 and 155 °C (solid and dashed lines, respectively). c) Maximum g-factor value in consecutive heating/cooling cycles of OIM_Au15_dopR (up) and OIM_Au15_dopS (down). d) Schematic representation of the behavior of OIM-based nanocomposites comprising NRs on thermal melting/freezing. e) CD spectra for OIM-based nanocomposites comprising Au NRs and either dopR (blue line) or dopS (red line) at 25 and 155 °C (solid and dashed lines, respectively). f) Maximum g-factor values in consecutive heating/cooling cycles for OIM-based nanocomposites comprising Au NRs, for samples and either with dopR (up) or dopS (down).

lack of CD signals at ≈400 nm agrees with our previous assignment of this signal to the formation of HNFs. The lack of CD signals in the plasmonic range suggests that NPs do not form chiral assemblies without the guidance of HNFs, and evidence that the discussed PCD signals do not originate from chirality transfer between the chiral dopant and NPs. After cooling the mixtures down to 25 °C, CD signatures from HNFs and helically arranged NPs were visible. To test the reversibility of CD switching, we performed 5 consecutive heating/cooling cycles, with a heating rate of 70 K min⁻¹, which took ≈2 min for the material to melt and for the PCD response to vanish, and a cooling rate of 20 K min⁻¹, which translated into ≈6–7 min for recovering the helical structure of the nanocomposite and thus its chiral plasmonic response, as shown in Figure 5c,f, in which g-factor values for the material were plotted. Notably, the g-factor values determined at the PCD peaks slightly vary and are 2–6 times stronger than those reported above, without limiting the probed sample area, which suggests that more homogenous regions were illuminated in this case. The g-factor values achieved here are similar to those reported in the literature,[70,71] however one or two orders of magnitude lower than the very recent state-of-the art examples using amyloid proteins or DNA-based assembly.[72,73] It should also be mentioned that recent effort has been devoted to solid-state supported systems, ensuring high g-factor values, however often beyond the visible range, for example, prepared by the deposition of chiral units onto substrates (g-factors of 0.3 at 385 nm and 0.2 at 800 nm[74]), or by deformation[75] and stacking[76] of nonchiral Au NPs (g-factors of 0.72 in the near-IR).

In the context of achieving higher g-values in the visible range, the performed optical modelling directs our attention toward optimizing the characteristic of constituents to increase length of the helical assemblies (Figure 4g) and achieving direc-

tional control over HNF growth[77] (Figures S37 and S38, Supporting Information).

## 2.5. Thermal Imprinting and Transfer of Chiral Thin Films

Confirmation of the switchable PCD signal upon melting/freezing cycles suggested the feasibility of further modifications based on soft-lithography methods.[78] A post-processing step of potential interest would comprise imposing a microscale pattern on the originally dropcasted samples, aiming at hierarchical structuring of the material. Similar patterning strategies have been employed in the fields of photovoltaics[79] or semiconductor emitters.[80] Herein, thermal nanoimprinting was performed using patterned PDMS as a mold (**Figure 6**a), which was placed into contact with the film at 110 °C. Conformal contact between PDMS and the sample was ensured by manually applying a moderate pressure to the mold, which remained in contact with the sample until it was cooled down to room temperature from the isotropic phase (155 °C). The template consisted of wrinkles created upon oxidation of the PDMS layer by plasma treatment under mechanical stretching, followed by stress relaxation causing the buckling of the oxidized layer.[81] By these means, 1D periodical patterns were obtained, which were successfully transferred to the molten dropcasted nanocomposite, which could be macroscopically observed, as the sample displayed iridescence from light diffraction caused by the micropattern, similar to that in the PDMS mold used for imprinting (Figure 6b). Atomic force microscopy (AFM) analysis of the imprinted nanocomposite showed a distinctly patterned surface, with a wrinkle periodicity of about 500 nm, closely matching the one of the PDMS mold used for imprinting (Figure 6c, Figure S39,
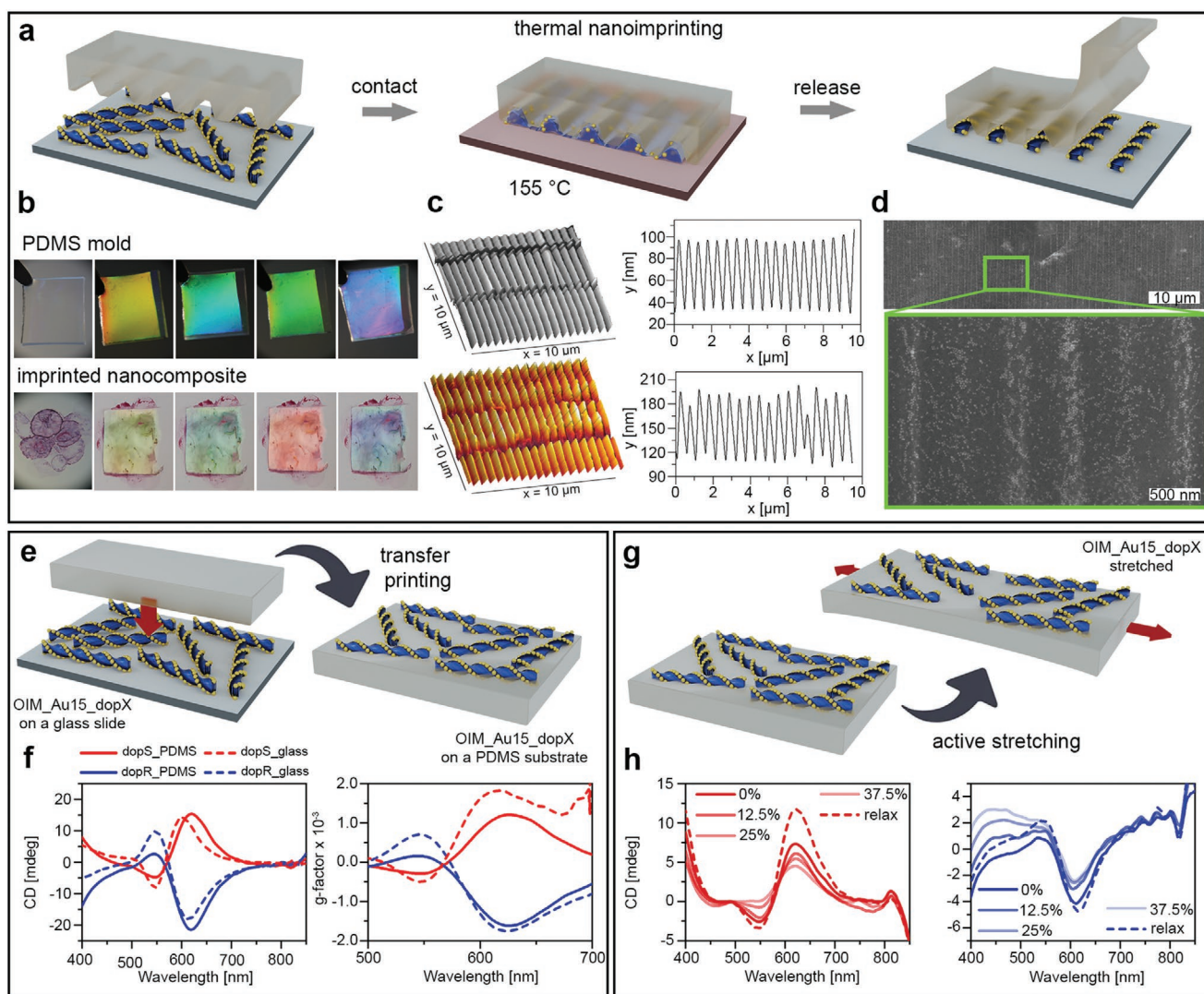
**ADVANCED
SCIENCE NEWS**
www.advancedsciencenews.com

**ADVANCED
FUNCTIONAL
MATERIALS**
www.afm-journal.de

**Figure 6.** Moldability of OIM-based chiral thin films. a) Schematic model of the thermal nanoimprinting process. b) Images of a 1 cm² wrinkled PDMS mold and OIM_Au15_dopX film before and after the imprinting process, displaying iridescence from light diffraction caused by the micropattern, viewed at different tilt angles. c) AFM topography images of a patterned PDMS mold (upper panel) and OIM_Au15_dopX film after nanoimprinting (lower panel), as well as, their respective surface height profiles. d) SEM images of an imprinted OIM_Au15_dopX sample. e) Schematic model of the transfer printing process. f) CD and g-factor spectra for OIM_Au15_dopR and OIM_Au15_dopS transferred onto a PDMS substrate, compared with measurements for OIM_Au15_dopX samples on a glass substrate. g) Schematic representation of the stretching process of OIM_Au15_dopX on a PDMS substrate. h) CD spectra for OIM_Au15_dopS (in red) and OIM_ Au15_dopR (in blue) on PDMS, for a gradually (0%, 12.5%, 25%, 37.5%, and 45%) stretched and relaxed nanocomposite.

Supporting Information). SEM analysis of the material additionally confirmed a periodic structure on a large area of the sample, while CD measurements (Figure 6d, Figures S39 and S42, Supporting Information) proved the formation of chiral assemblies in the wrinkles. The thermal nanoimprinting principle was also applied for different pattern types (Note S8, Figure S41, Supporting Information) and the appearance of extrinsic effects from the grating was confirmed by angle-dependent CD characterization (Note S9, Figure S42, Supporting Information), which is interesting given the recent interest in films exhibiting multiple anisotropies.[29]

Furthermore, the versatility of OIM-based chiral thin films is reasserted by their transfer printing[82] from the initial glass slide onto a PDMS target substrate. To do so, the dropcasted film was pressed and rubbed with the PDMS substrate when melted, followed by fast lift-off, resulting in partial transfer of the material (Figure 6e, Figure S43, Supporting Information). The transferred sample maintains the initial PCD properties, in terms of comparable CD and g-factor values to those of samples measured on glass substrates (Figure 6f). However, the CD spectra of the transferred sample (OIM_Au15_dopX_ PDMS) showed a minor widening of the registered CD bands. Mechanical endurance of the transferred nanocomposite was tested by measuring its chiroptical response during controlled stretching of the flexible substrate (Figure 6g). Using a homemade device (Figure S44, Supporting Information) we

performed CD measurements of the OIM-based chiral thin film on a PDMS substrate for percent strain values of 0%, 12.5%, 25%, and 37.5%, taking a stretched PDMS substrate with no composite on it as reference (Figure 6h). Importantly, even though a gradual loss of CD intensity was observed for increasing mechanical stress, the chiroptical response was recovered upon relaxation, again demonstrating the dynamic character of the material.

## 3. Conclusions

In summary, the work presented here describes a simple strategy for fabricating centimeter-scale chiral plasmonic films made of Au nanoparticles and liquid crystals, exhibiting a reversibly reconfigurable structure and controllable chiroptical properties. In this method, the chirality of a minute amount of an organic dopant is amplified by the LC molecules assembling into helical nanofibers, which then transfer the chirality onto achiral Au NPs, by guiding their assembly. Combined UV–vis, CD, TEM, SEM, and theoretical modeling revealed the interactions of composite constituents and details of their structure. PCD films are easily realized with different sizes of Au NPs, enabling tuning the PCD wavelengths with high dissymmetry factors up to $6 \times 10^{-3}$. Reversible melting of the material allows active control over PCD properties in thin film configurations and the realization of patterned films using PDMS-based soft lithography, without the requirement of using any solvents. Transfer printing of the films onto a flexible substrate is demonstrated, thereby broadening the active behavior of the material with mechanical tunability. The work presented here reveals a way to combine thermal responsiveness of LC materials and plasmonic coupling of achiral plasmonic NPs, resulting in a useful methodology to achieve tunable and moldable PCD thin films which may hold significant potential in future active, flexible chiroptical materials.

## 4. Experimental Section

*Materials*: All the starting materials were purchased from Sigma-Aldrich and were used without any further purification. PDMS precursors (Dow Sylgard 184 Silicone Elastomer Kit) were obtained from Ellsworth Adhesives.

*Nanoparticle Synthesis and Surface Functionalization*: The syntheses for Au4, Au6, Au10, Au15, and Au20 were conducted according to the literature methods, more details on the synthesis and surface functionalization procedures can be found in Note S5, Supporting Information.[61–64]

*Nanocomposite Preparation*: In a typical nanocomposite preparation procedure 53.0 µL of 2.5 mM Au15 THF solution was added to 450 µL of 0.43 mg mL$^{-1}$ THF solution of OIM and 45 µL of 0.43 mg mL$^{-1}$ THF solution of dopX. The mixture was slowly dropcasted to a standard (10 mm x 10 mm) glass slide kept at 70 °C, then quickly (70 K min$^{-1}$) heated above the melting point (155 °C) and cooled down to room temperature with the controlled rate of 20 K min$^{-1}$. The melting and freezing were realized using a FTIR600 SP Linkam stage with T96 LinkPad system controller, available at the University of Warsaw.

*PDMS Substrates Preparation*: Typically, PDMS cross-linker and precursor were used in a ratio of (1:20), mixed thoroughly, degassed for 30 min under vacuum, and finally drop casted on a petri dish.

After thermal curing at 60 °C overnight, 1 cm$^2$ pieces were cut, rinsed with Milli-Q water and dried with nitrogen, for transfer printing experiments. PDMS mold preparation: 5:1 precursor to cross-linker ratio was used to fabricate PDMS substrates of 1.5 mm of thickness. After the typical experimental procedure, 3.5 cm × 1 cm piece was cut and clamped in a homemade stretching device, leaving an exposed area of 1 cm$^2$. Under a strain of 40%, the PDMS sample was oxidized under oxygen plasma (Pico, Diener Electronic, Germany) for 7 min, at 0.4 mbar and under a plasma power of 200 W. After the treatment, mechanical stretch was released provoking the wrinkling of the vitrified surface.

*Structural Characterization*: The shape and size of nanoparticles, as well as, their self-assembly into helical structures, were examined by TEM (JEOL-1400, JEOL Co. Japan), equipped with high-resolution digital camera CCD MORADA G2 (EMSIS GmbH, Germany) available at the Nencki Institute of Experimental Biology of Polish Academy of Sciences, Laboratory of Electron Microscopy. In addition, the structure of the OIM and OIM_dopX nanocomposites was analyzed via SEM using the FE-SEM/EDS, available at the Faculty of Chemistry, University of Warsaw. The imaging was realized on ITO wafers. AFM height images were acquired in tapping mode using the NanoWizard II microscope (JPK, Bruker), available at CIC biomaGUNE, and were analyzed with the software Gwyddion.

*Optical Characterization*: Spectroscopic study of the materials in the colloid in the UV–vis range were performed using GENESYS 50 UV–vis spectrometer, available at University of Warsaw. The spectra of the functionalized nanoparticles were performed in THF solutions, using quartz cuvettes with a 2 mm optical path. The liquid crystalline material was probed with POM, Zeiss Axio Imager Am.2 microscope, available at the University of Warsaw. Circular Dichroism measurements were performed using Chirascan Circular Dichroism Spectrometer by Applied PhotoPhysics, available at the University of Warsaw, and the JASCO J-1500 Circular Dichroism Spectrometer available at CIC biomaGUNE. The data are not corrected for reflection.

*Theoretical Modeling*: All of the details regarding theoretical modeling can be found in Note S4, Supporting Information.

## Supporting Information

Supporting Information is available from the Wiley Online Library or from the author.

## Acknowledgements

## Conflict of Interest

The authors declare no conflict of interest.

## Data Availability Statement

The data that support the findings of this study are available from the corresponding author upon reasonable request.

## Keywords

chiral plasmonics, chirality transfer, dynamic self-assembly, gold nanoparticles, nanoarchitectonics

[1] P. Li, J. Deng, *Adv. Funct. Mater.* **2021**, *31*, 2105315.

[2] P. Lv, X. Lu, L. Wang, W. Feng, *Adv. Funct. Mater.* **2021**, *31*, 2104991.

[3] P. Rofouie, E. Galati, L. Sun, A. S. Helmy, E. Kumacheva, *Adv. Funct. Mater.* **2019**, *29*, 1905552.

[4] A. Nych, J. I. Fukuda, U. Ognysta, S. Zumer, I. Mušević, *Nat. Phys.* **2017**, *13*, 1215.

[5] C. J. Kim, A. Sánchez-Castillo, Z. Ziegler, Y. Ogawa, C. Noguez, J. Park, *Nat. Nanotechnol.* **2016**, *11*, 520.

[6] G. Albano, G. Pescitelli, L. Di Bari, *Chem. Rev.* **2020**, *120*, 10145.

[7] L. Wan, J. Wade, F. Salerno, O. Arteaga, B. Laidlaw, X. Wang, T. Penfold, M. J. Fuchter, A. J. Campbell, *ACS Nano* **2019**, *13*, 8099.

[8] Z.-W. Luo, L. Tao, C.-L. Zhong, Z.-X. Li, K. Lan, Y. Feng, P. Wang, H.-L. Xie, *Macromolecules* **2020**, *53*, 9758.

[9] N. Y. Kim, J. Kyhm, H. Han, S. J. Kim, J. Ahn, D. K. Hwang, H. W. Jang, B.-K. Ju, J. A. Lim, *Adv. Funct. Mater.* **2019**, *29*, 1808668.

[10] U. R. Gabinet, C. O. Osuji, *Nano Res.* **2019**, *12*, 2172.

[11] S. Link, G. V. Hartland, *J. Phys. Chem. C* **2021**, *125*, 10175.

[12] N. A. Kotov, L. M. Liz-Marzán, P. S. Weiss, *ACS Nano* **2021**, *15*, 12457.

[13] H. E. Lee, H. Y. Ahn, J. Mun, Y. Y. Lee, M. Kim, N. H. Cho, K. Chang, W. S. Kim, J. Rho, K. T. Nam, *Nature* **2018**, *556*, 360.

[14] W. Ma, L. Xu, A. F. De Moura, X. Wu, H. Kuang, C. Xu, N. A. Kotov, *Chem. Rev.* **2017**, *117*, 8041.

[15] J. Kumar, K. G. Thomas, L. M. Liz-Marzán, *Chem. Commun.* **2016**, *52*, 12555.

[16] Y. Sang, J. Han, T. Zhao, P. Duan, M. Liu, *Adv. Mater.* **2020**, *32*, 1900110.

[17] B. Zhao, X. Gao, K. Pan, J. Deng, *ACS Nano* **2021**, *15*, 7463.

[18] J.-X. Gao, W.-Y. Zhang, Z.-G. Wu, Y.-X. Zheng, D.-W. Fu, *J. Am. Chem. Soc.* **2020**, *142*, 4756.

[19] M. Zhou, Y. Sang, X. Jin, S. Chen, J. Guo, P. Duan, M. Liu, *ACS Nano* **2021**, *15*, 2753.

[20] X. Yang, M. Zhou, Y. Wang, P. Duan, *Adv. Mater.* **2020**, *32*, 2000820.

[21] G. Zheng, J. He, V. Kumar, S. Wang, I. Pastoriza-Santos, J. Pérez-Juste, L. M. Liz-Marzán, K. Y. Wong, *Chem. Soc. Rev.* **2021**, *50*, 3738.

[22] S. W. Im, H. Ahn, R. M. Kim, N. H. Cho, H. Kim, Y. Lim, H. Lee, K. T. Nam, *Adv. Mater.* **2020**, *32*, 1905758.

[23] M. J. Urban, C. Shen, X. T. Kong, C. Zhu, A. O. Govorov, Q. Wang, M. Hentschel, N. Liu, *Annu. Rev. Phys. Chem.* **2019**, *70*, 275.

[24] J. Cheng, E. H. Hill, Y. Zheng, T. He, Y. Liu, *Mater. Chem. Front.* **2018**, *2*, 662.

[25] S. W. Hsu, A. L. Rodarte, M. Som, G. Arya, A. R. Tao, *Chem. Rev.* **2018**, *118*, 3100.

[26] F. Neubrech, M. Hentschel, N. Liu, *Adv. Mater.* **2020**, *32*, 1905640.

[27] W. Zhao, W. Zhang, R. Wang, Y. Ji, X. Wu, X. Zhang, *Adv. Funct. Mater.* **2019**, *29*, 1900587.

[28] X. Lan, T. Liu, Z. Wang, A. O. Govorov, H. Yan, Y. Liu, *J. Am. Chem. Soc.* **2018**, *140*, 11763.

[29] J. Gao, W. Wu, V. Lemaire, A. Carvalho, S. Nlate, T. Buffeteau, R. Oda, Y. Battie, M. Pauly, E. Pouget, *ACS Nano* **2020**, *14*, 4111.

[30] J. Guo, J. Y. Kim, S. Yang, J. Xu, Y. C. Choi, A. Stein, C. B. Murray, N. A. Kotov, C. R. Kagan, *ACS Photonics* **2021**, *8*, 1286.

[31] J. Bai, Y. Yao, *ACS Nano* **2021**, *15*, 14263.

[32] P. T. Probst, M. Mayer, V. Gupta, A. M. Steiner, Z. Zhou, G. K. Auernhammer, T. A. F. König, A. Fery, *Nat. Mater.* **2021**, *20*, 1024.

[33] I. Gharbi, V. Palacio-Betancur, H. Ayeb, D. Demaille, J. J. de Pablo, R. D. Kamien, E. Lacaze, *ACS Appl. Nano Mater.* **2021**, *4*, 6700.

[34] L. Wang, A. M. Urbas, Q. Li, *Adv. Mater.* **2020**, *32*, 1801335.

[35] H. Mundoor, B. Senyuk, I. I. Smalyukh, *Science* **2016**, *352*, 69.

[36] Q. Liu, Y. Yuan, I. I. Smalyukh, *Nano Lett.* **2014**, *14*, 4071.

[37] S.-P. Do, A. Missaoui, A. Coati, D. Coursault, H. Jeridi, A. Resta, N. Goubet, M. M. Wojcik, A. Choux, S. Royer, E. Briand, B. Donnio, J. L. Gallani, B. Pansu, E. Lhuillier, Y. Garreau, D. Babonneau, M. Goldmann, D. Constantin, B. Gallas, B. Croset, E. Lacaze, *Nano Lett.* **2020**, *20*, 1598.

[38] D. P. N. Gonçalves, T. Hegmann, *Angew. Chem., Int. Ed.* **2021**, *60*, 17344.

[39] W. Lewandowski, N. Vaupotič, D. Pociecha, E. Górecka, L. M. Liz-Marzán, *Adv. Mater.* **2020**, *32*, 1905591.

[40] C. N. Melton, S. T. Riahinasab, A. Keshavarz, B. J. Stokes, L. S. Hirst, *Nanomaterials* **2018**, *8*, 146.

[41] M. Bagiński, M. Tupikowska, G. González-Rubio, M. Wójcik, W. Lewandowski, *Adv. Mater.* **2020**, *32*, 1904581.

[42] P. Bai, S. Yang, W. Bao, J. Kao, K. Thorkelsson, M. Salmeron, X. Zhang, T. Xu, *Nano Lett.* **2017**, *17*, 6847.

[43] P. Szustakiewicz, N. Kowalska, D. Grzelak, T. Narushima, M. Góra, M. Bagiński, D. Pociecha, H. Okamoto, W. Lewandowski, L. M. Liz-Marzán, *ACS Nano* **2020**, *14*, 12918.

[44] L. Scarabelli, D. Vila-Liarte, A. Mihi, L. M. Liz-Marzán, *Acc. Mater. Res.* **2021**, *2*, 816.

[45] S. Zhu, Y. Tang, C. Lin, X. Y. Liu, Y. Lin, *Small Methods* **2021**, *5*, 2001060.

[46] D. A. Coleman, J. Fernsler, N. Chattham, M. Nakata, Y. Takanishi, E. Körblova, D. R. Link, R.-F. Shao, W. G. Jang, J. E. Maclennan, O. Mondainn-Monval, C. Boyer, W. Weissflog, G. Pelzl, L.-C. Chien, J. Zasadzinski, J. Watanabe, D. M. Walba, H. Takezoe, N. A. Clark, *Science* **2003**, *301*, 1204.

[47] L. E. Hough, M. Spannuth, M. Nakata, D. A. Coleman, C. D. Jones, G. Dantlgraber, C. Tschierske, J. Watanabe, E. Körblova, D. M. Walba, J. E. Maclennan, M. A. Glaser, N. A. Clark, *Science* **2009**, *325*, 452.

[48] L. E. Hough, H. T. Jung, D. Krüerke, M. S. Heberling, M. Nakata, C. D. Jones, D. Chen, D. R. Link, J. Zasadzinski, G. Heppke, J. P. Rabe, W. Stocker, E. Körblova, D. M. Walba, M. A. Glaser, N. A. Clark, *Science* **2009**, *325*, 456.

[49] S. Shadpour, A. Nemati, N. J. Boyd, L. Li, M. E. Prevot, S. L. Wakerlin, J. P. Vanegas, M. Salomończyk, E. Hegmann, C. Zhu, M. R. Wilson, A. I. Jakli, T. Hegmann, *Mater. Horiz.* **2019**, *6*, 959.

[50] C. Zhang, N. Diorio, O. D. Lavrentovich, A. Jákli, *Nat. Commun.* **2014**, *5*, 3302.

[51] L. E. Hough, H. T. Jung, D. Krüerke, M. S. Heberling, M. Nakata, C. D. Jones, D. Chen, D. R. Link, J. Zasadzinski, G. Heppke, J. P. Rabe, W. Stocker, E. Körblova, D. M. Walba, M. A. Glaser, N. A. Clark, *Science* **2009**, *325*, 456.

[52] W. Park, T. Ha, T.-T. Kim, A. Zep, H. Ahn, T. J. Shin, K. I. Sim, T. S. Jung, J. H. Kim, D. Pociecha, E. Gorecka, D. K. Yoon, *NPG Asia Mater* **2019**, *11*, 45.

[53] W. Park, D. K. Yoon, *Crystals* **2020**, *10*, 675.

[54] M. Urbańska, P. Morawiak, M. Czerwiński, *J. Mol. Liq.* **2020**, *309*, 113141.

**ADVANCED
SCIENCE NEWS**

www.advancedsciencenews.com

**ADVANCED
FUNCTIONAL
MATERIALS**

www.afm-journal.de

[55] H. Hayashi, A. Wang, K. Kawabata, H. Goto, *Mater. Chem. Phys.* **2013**, *137*, 816.

[56] L. Li, M. Salamończyk, S. Shadpour, C. Zhu, A. Jákli, T. Hegmann, *Nat. Commun.* **2018**, *9*, 714.

[57] P. Lesiak, K. Bednarska, W. Lewandowski, M. Wójcik, S. Polakiewicz, M. Bagiński, T. Osuch, K. Markowski, K. Orzechowski, M. Makowski, J. Bolek, T. R. Woliński, *ACS Nano* **2019**, *13*, 10154.

[58] H. Yu, C. Welch, W. Qu, C. J. Schubert, F. Liu, G. Siligardi, G. H. Mehl, *Mater. Horiz.* **2020**, *7*, 3021.

[59] W. Zhang, M. F. Prodanov, J. Schneider, S. K. Gupta, T. Dudka, V. V. Vashchenko, A. L. Rogach, A. K. Srivastava, *Adv. Funct. Mater.* **2019**, *29*, 1805094.

[60] D. Vila-Liarte, N. A. Kotov, L. M. Liz-Marzán, *Chem. Sci.* **2021**, *12*, 03327a.

[61] Y. Chen, X. Wang, *Mater. Lett.* **2008**, *62*, 2215.

[62] W. Zhu, R. Michalsky, Ö. Metin, H. Lv, S. Guo, C. J. Wright, X. Sun, A. A. Peterson, S. Sun, *J. Am. Chem. Soc.* **2013**, *135*, 16833.

[63] G. González-Rubio, V. Kumar, P. Llombart, P. Díaz-Núñez, E. Bladt, T. Altantzis, S. Bals, O. Peña-Rodríguez, E. G. Noya, L. G. Macdowell, A. Guerrero-Martínez, L. M. Liz-Marzán, *ACS Nano* **2019**, *13*, 4424.

[64] Y. Zheng, X. Zhong, Z. Li, Y. Xia, *Part. Part. Syst. Charact.* **2014**, *31*, 266.

[65] D. Grzelak, P. Szustakiewicz, C. Tollan, S. Raj, P. Král, W. Lewandowski, L. M. Liz-Marzán, *J. Am. Chem. Soc.* **2020**, *142*, 18814.

[66] M. I. Mishchenko, L. D. Travis, D. W. Mackowski, *J. Quant. Spectrosc. Radiat. Transfer* **1996**, *55*, 535.

[67] P. Liu, Y. Battie, M. Decossas, S. Tan, E. Pouget, Y. Okazaki, T. Sagawa, R. Oda, *ACS Nano* **2021**, *15*, 16411.

[68] P. Liu, Y. Battie, Y. Okazaki, N. Ryu, E. Pouget, S. Nlate, T. Sagawa, R. Oda, *Chem. Commun.* **2021**, *57*, 12024.

[69] R. Schreiber, N. Luong, Z. Fan, A. Kuzyk, P. C. Nickels, T. Zhang, D. M. Smith, B. Yurke, W. Kuang, A. O. Govorov, T. Liedl, *Nat. Commun.* **2013**, *4*, 2948.

[70] J. Kumar, H. Eraña, E. López-Martínez, N. Claes, V. F. Martín, D. M. Solís, S. Bals, A. L. Cortajarena, J. Castilla, L. M. Liz-Marzán, *Proc. Natl. Acad. Sci. U. S. A.* **2018**, *115*, 3225.

[71] A. Kuzyk, R. Schreiber, Z. Fan, G. Pardatscher, E. M. Roller, A. Högele, F. C. Simmel, A. O. Govorov, T. Liedl, *Nature* **2012**, *483*, 311.

[72] S. Mokashi-Punekar, Y. Zhou, S. C. Brooks, N. L. Rosi, *Adv. Mater.* **2020**, *32*, 201905975.

[73] J. Lu, Y. Xue, K. Bernardino, N. N. Zhang, W. R. Gomes, N. S. Ramesar, S. Liu, Z. Hu, T. Sun, A. F. de Moura, N. A. Kotov, K. Liu, *Science* **2021**, *371*, 1368.

[74] W. Wu, Y. Battie, V. Lemaire, G. Decher, M. Pauly, *Nano Lett.* **2021**, *21*, 8298.

[75] Y. Kim, B. Yeom, O. Arteaga, S. J. Yoo, S. G. Lee, J. G. Kim, N. A. Kotov, *Nat. Mater.* **2016**, *15*, 461.

[76] P. T. Probst, M. Mayer, V. Gupta, A. M. Steiner, Z. Zhou, G. K. Auernhammer, T. A. F. König, A. Fery, *Nat. Mater.* **2021**, *20*, 1024.

[77] W. Park, D. K. Yoon, *Crystals* **2020**, *10*, 675.

[78] D. Qin, Y. Xia, G. M. Whitesides, *Nat. Protoc.* **2010**, *5*, 491.

[79] M. Gibert-Roca, P. Molet, A. Mihi, M. Campoy-Quiles, *J. Mater. Chem. C* **2020**, *8*, 9688.

[80] D. Vila-Liarte, M. W. Feil, A. Manzi, J. L. Garcia-Pomar, H. Huang, M. Döblinger, L. M. Liz-Marzán, J. Feldmann, L. Polavarapu, A. Mihi, *Angew. Chem., Int. Ed.* **2020**, *59*, 17750.

[81] A. Schweikart, A. Fery, *Microchim. Acta* **2009**, *165*, 249.

[82] M. A. Meitl, Z. T. Zhu, V. Kumar, K. J. Lee, X. Feng, Y. Y. Huang, I. Adesida, R. G. Nuzzo, J. A. Rogers, *Nat. Mater.* **2006**, *5*, 33.

**2111280** (12 of 12)